

Hyperfine Structure and Coherent Dynamics of Rare-Earth Spins Explored with Electron-Nuclear Double Resonance at Subkelvin Temperatures

Pei-Yun Li,^{1,2} Chao Liu,^{1,2} Zong-Quan Zhou,^{1,2,*} Xiao Liu,^{1,2} Tao Tu,^{1,2} Tian-Shu Yang,^{1,2} Zong-Feng Li,^{1,2} Yu Ma,^{1,2} Jun Hu,^{1,2} Peng-Jun Liang,^{1,2} Xue Li,^{1,2} Jian-Yin Huang,^{1,2} Tian-Xiang Zhu,^{1,2} Chuan-Feng Li^{1,2,†} and Guang-Can Guo^{1,2}

¹*CAS Key Laboratory of Quantum Information, University of Science and Technology of China, Chinese Academy of Sciences, Hefei, 230026, China*

²*CAS Center for Excellence in Quantum Information and Quantum Physics, University of Science and Technology of China, Hefei, 230026, China*



(Received 13 January 2019; revised manuscript received 15 January 2020; accepted 22 January 2020; published 28 February 2020)

An experimental platform for ultralow-temperature pulsed ENDOR spectroscopy is constructed for general bulk materials. Coherent properties of the coupled electron and nuclear spins of rare-earth dopants in a crystal ($^{143}\text{Nd}^{3+}:\text{Y}_2\text{SiO}_5$) are investigated from 100 mK to 6 K. At the lowest working temperatures, two-pulse-echo coherence times exceeding 2 and 40 ms are achieved for the electron and nuclear spins, while the electronic Zeeman and hyperfine population lifetimes are more than 15 s and 10 min. With the aid of the near-unity electron spin polarization at 100 mK, the complete hyperfine-level structure with 16 energy levels is measured by the ENDOR technique without the assistance of the reconstructed spin Hamiltonian. These results demonstrate the suitability of deeply cooled paramagnetic rare-earth ions for memory components aimed at quantum communication and quantum computation. The experimental platform developed is expected to be a powerful tool for study of paramagnetic materials in various research fields.

DOI: [10.1103/PhysRevApplied.13.024080](https://doi.org/10.1103/PhysRevApplied.13.024080)

I. INTRODUCTION

Electron-coupled nuclear spins in solids are promising candidates for the memory components in quantum computation and quantum communication. The electron spins can be dedicated to interface with superconducting circuits [1–3], while long-term storage is provided by the nuclear spins to access much-longer coherence lifetimes [4,5]. Arbitrary qubit states can be coherently transferred between the electron and nuclear spins with high fidelity [6,7]. Large storage bandwidth is promised by the gigahertz-range electronic Zeeman and electron-nuclear hyperfine interactions [4,8–10]. This is also an appealing physical platform for the realization of optical quantum memory at telecom wavelengths with sufficient storage time and efficiency [4].

Although there is general interest in lowering working temperatures to decelerate the decoherence processes [5,7,11], coherent properties of the electron-coupled-nuclear-spin systems at subkelvin temperatures are still not clear. As a basic tool, the coherent dynamics of the coupled electron and nuclear spins can be investigated with pulsed ENDOR spectroscopy [6,12,13], which

has been conducted only at liquid-helium temperature for bulk materials. In this work, we achieve a comprehensive enhancement of the population and coherence lifetimes of both the electron spins and the coupled nuclear spins. The measurements are based on pulsed EPR and ENDOR spectroscopy at temperatures down to 100 mK when the electron spins are almost fully polarized. Rare-earth-ion-doped solids, the model system studied herein, are state-of-the-art candidate material for optical quantum memory [14–19] with the potential for microwave memory [7] and microwave-to-optical quantum transduction [20,21]. For rare-earth-ion-doped solids at subkelvin temperatures, there have previous studies of the optical coherence lifetimes [10,22,23], but reports on the coherent spin dynamics are rare [24,25]. In this work, as the sample temperature is reduced to the subkelvin region, the growth of spin relaxation and coherence times is observed to accelerate simultaneously. In addition, with the aid of the near-unity polarization of the electron spins, the complete hyperfine structure of the ground state of $^{143}\text{Nd}^{3+}:\text{Y}_2\text{SiO}_5$ is experimentally resolved via a series of alternative pulsed ENDOR sequences.

This paper is organized as follows. Section II describes the construction of the experimental platform and the verification of the sample temperature. Section III describes the experimental process to directly measure

*zq_zhou@ustc.edu.cn

†cfli@ustc.edu.cn

the ground-state hyperfine-level structure by a modified pulsed ENDOR technique. Section IV describes the reconstruction of the spin Hamiltonian. Section V discusses the coherent electron and nuclear spin dynamics of $^{143}\text{Nd}^{3+}:\text{Y}_2\text{SiO}_5$ over a large temperature range from 100 mK to 6 K.

II. EXPERIMENTAL SETUP AND TEMPERATURE VERIFICATION

The sample, an Y_2SiO_5 crystal doped with isotopically purified $^{143}\text{Nd}^{3+}$ ions of 20 ppm (Laser Crylink), is mounted inside a modified cylindrical dielectric resonator (Bruker EN4118X-MD4) with a copper head integrated with its shell above the sample space. The crystal is cut along its D_1 , D_2 , and b axes with dimensions of $1.2 \times 1.0 \times 1.4 \text{ mm}^3$. There are some even Nd isotopes remaining in the crystal since the enrichment of ^{143}Nd is greater than 91% in the starting material. Thermal conduction to the crystal is provided by two rods made of high-purity single-crystal silicon [26]; see Fig. 1(a).

The EPR resonance frequency $f_r = 9.56 \text{ GHz}$. Cooling of the sample and the ENDOR resonator is provided by a cryogen-free dilution refrigerator (Triton 400, Oxford Instruments). The electromagnet is installed separately from the dilution refrigerator on a rotary table that is portable along a guided rail. Unless otherwise stated, the orientation of the magnetic field B_0 is close to the D_1 optical extinction axis of the crystal (within an error of approximately 2°). Microwave and radio-frequency (rf) pulses with peak powers of 20 and 100 W, respectively, are used to coherently drive the electron and nuclear spin ensembles, respectively. To eliminate heating induced by the background noise of the microwave and rf amplifiers, transistor-transistor logic circuits are used to invalidate

the amplifiers unless there are pulses injected into them. To avoid excessive Ohm heating in the coaxial cables, superconducting coaxial cables (NbTiNbTi085 and NbTiNbTi047 , Keycom) are used below the 4-K stage. In addition, 0-dB attenuators are inserted to heat-sink the inner and outer conductors.

The need for high power is thought to be a major challenge when one is performing pulsed EPR and ENDOR experiments at subkelvin temperatures [27]. Therefore, verification of the sample temperature is indispensable. Preliminarily, the integrated area of the electron spin echo (ESE), which is proportional to the electron spin polarization $P_e = \tanh(hf_r/2k_B T)$, is used to calibrate the sample temperature. Here h is the Planck constant, k_B is the Boltzmann constant, and T represents the sample temperature. To take advantage of the simple level structure of a standard spin-1/2 system, B_0 is set to 458.2 mT. The remaining even isotopes of Nd^{3+} with $I = 0$ are addressed [see Fig. 3(a)]. ESE is produced by conventional two-pulse-echo sequences. The π pulses are 48 ns in length, and τ is set to 1 μs , much shorter than the electron spin coherence time. It can be observed from Fig. 1(b) that the integrated area of ESE at various temperatures agrees very well with the fitted line. At 100 mK, an electron spin polarization of 98% is achieved. In this regime the cross relaxation among the electron spins can be negligible [28,29].

The sample temperature is also verified by means of the dynamical process of the electron spins. The electron spin relaxation time T_{1e} is measured with inversion-recovery sequences. Its temperature dependence can be modeled with the well-established spin lattice relaxation (SLR) mechanism that is detailed in Sec. IV. We use the T_{1e} data at higher temperatures from 2 to 6.5 K to generate the fitted curve in Fig. 1(c), and extrapolate it down to 100 mK. T_{1e} recorded at lower temperatures perfectly follows

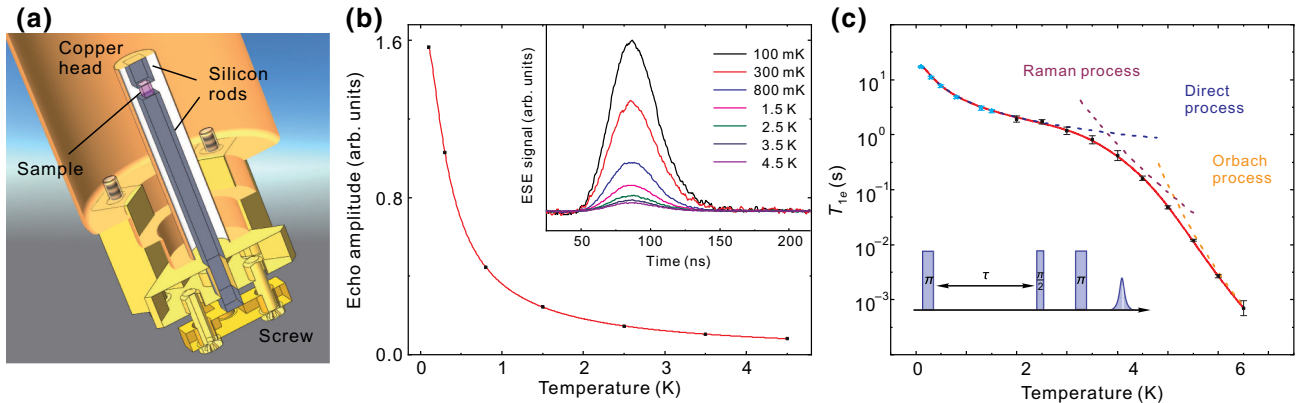


FIG. 1. (a) Thermal-conduction components around and inside the ENDOR resonator. Stress can be applied to the sample by the screw for better thermal contact. (b) Temperature dependence of the integrated area of ESE. The red line is the fit to a Boltzmann distribution. Profiles of the echoes recorded at various temperatures are shown in the inset. (c) Temperature dependence of T_{1e} for even isotopes of Nd^{3+} with $I = 0$. The solid red line is the fitted curve based on the spin-lattice relaxation model and the T_{1e} data above 2 K. The cyan stars represent T_{1e} measured below 2 K. The contributions from the direct, Raman, and Orbach processes are also displayed independently with dashed curves colored blue, purple, and orange, respectively.

this predicted curve. The longest T_{1e} of 17 s is obtained at 100 mK, which has reached the limit imposed by the spontaneous emission of phonons [30,31].

III. DIRECT MEASUREMENT OF HYPERFINE-LEVEL STRUCTURE

Taking advantage of the ultralow sample temperature, here we develop a series of ENDOR sequences to directly measure the complete ground-state hyperfine-level structure of $^{143}\text{Nd}^{3+}:\text{Y}_2\text{SiO}_5$. The method is free from additional optical transitions [4,8] or the reconstructed spin Hamiltonians [33,34], as required in previous studies. A guideline is given in Fig. 2.

The field-swept ESE spectrum is given in Fig. 3(a). It is recorded at 6.0 K with B_0 close to the D_1 axis. The 18 resonance lines come from Nd^{3+} located in two magnetically inequivalent classes that are related by C_2 symmetry along the crystal's b axis [7]. Each of the classes contains eight lines corresponding to $^{143}\text{Nd}^{3+}$ with a nuclear spin of $I = 7/2$, and one other line corresponding to even isotopes with $I = 0$. In this study we try to characterize the hyperfine-level structure at $B_0 = 402.7$ mT, when one of the EPR transitions is at resonance.

For a selected EPR transition, the “allowed” NMR transitions with $\Delta m_S = 0$ and $\Delta m_I = 1$ can be detected by

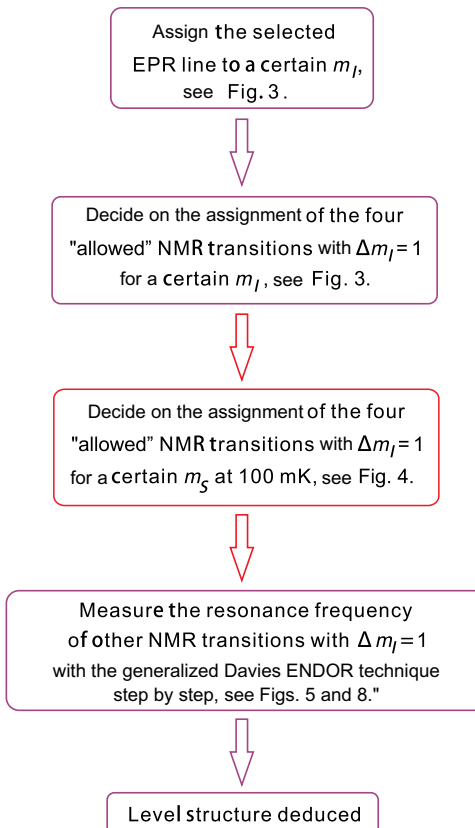


FIG. 2. The procedures for the determination of the ground-state hyperfine-level structure of $^{143}\text{Nd}^{3+}:\text{Y}_2\text{SiO}_5$.

Davies ENDOR sequences [35]. Here we use the ket $|m_S, m_I\rangle$ to denote the electron and nuclear spin projections. The ENDOR spectra measured at 402.7 and 358.2 mT are shown in Figs. 3(b) and 3(c), respectively. It can be seen that the two resonance peaks located at approximately 165 and 172 MHz coexist in the two spectra, indicating that these two lines correspond to the $^{143}\text{Nd}^{3+}$ ions located in the same magnetically inequivalent class. By comparison of Davies ENDOR results acquired at various resonant magnetic fields, all eight EPR lines corresponding to the same magnetically inequivalent class can be accordingly discriminated, as marked in Fig. 3(a). Consequently, it can be deduced that the 402.7-mT line corresponds to the EPR transition of $| -1/2, +3/2 \rangle \rightarrow | +1/2, +3/2 \rangle$. The

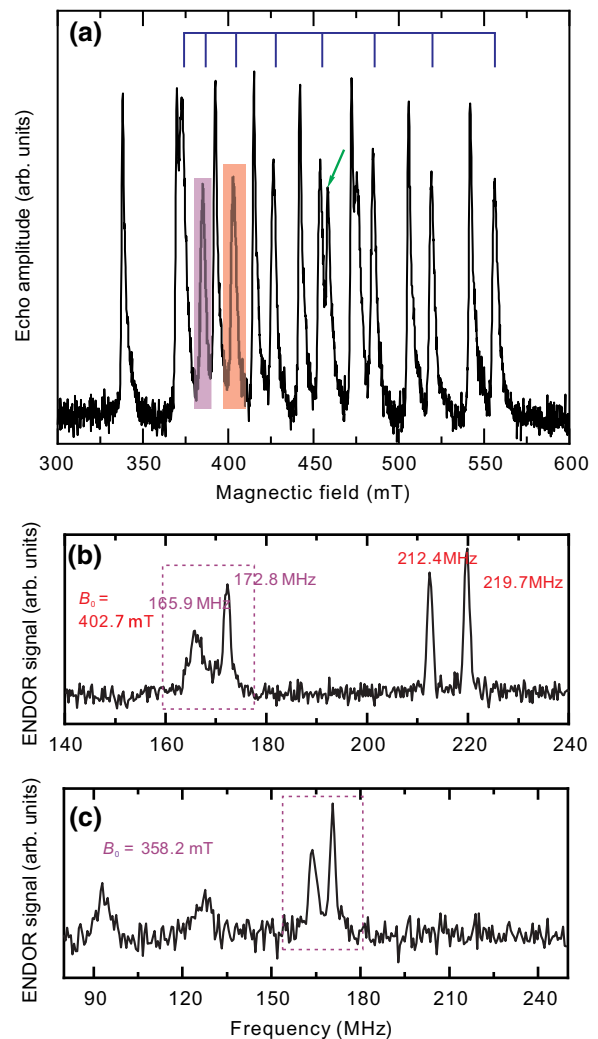


FIG. 3. (a) Results from the field-swept ESE experiment. The resonance line with $B_0 = 458.2$ mT used for temperature verification is marked with a green arrow. The hyperfine-level structure is determined at the EPR line with $B_0 = 402.7$ mT, which is shaded in red. The EPR line at 358.2 mT is shaded in purple. (b),(c) Davies ENDOR spectra recorded at $B_0 = 402.7$ mT and 358.2 mT, respectively.

two ENDOR lines located at 212.4 and 219.7 MHz, as shown in Fig. 2(b), correspond to the NMR transitions of $|m_S, +1/2\rangle \rightarrow |m_S, +3/2\rangle$, in which m_S can be $+1/2$ or $-1/2$.

A critical step is to decide the electron spin projection m_S for these lines [7,11,31]. This can be experimentally resolved at 100 mK when the electron spin is almost fully polarized. As shown in Fig. 4(a), nuclear spin polarization can then be established after the microwave and rf π pulses and subsequent waiting time $T_W = 60$ s. If the radio frequency is resonant with the NMR transition in the lower electron spin state ($m_S = -1/2$), nuclear spin coherence

can be created by a rf $\pi/2$ pulse and transferred to the electron spin [6]. Finally, an ESE signal can be observed. Otherwise, operations starting at the emptied energy level with $m_S = +1/2$ are ineffective. An illustration of the pulse sequence is given in Fig. S1 in Supplemental Material [31]. The experimental results are shown in Figs. 4(b)–4(e). The experimental phenomena are less clear for the NMR transitions of $|\pm 1/2, +3/2\rangle \rightarrow |\pm 1/2, +5/2\rangle$ at 165.9 and 172.8 MHz, possibly due to the imperfect rf excitation or the electron-nuclear cross relaxation. Nevertheless, the signal recorded without the initial nuclear spin polarization can be subtracted from the signal recorded at the end of the entire pulse sequence to acquire a standard echo profile. The experimental results indicate that the 212.4- and 172.8-MHz NMR transitions are in the lower electron spin level, corresponding to $m_S = -1/2$, while the 219.7- and 165.9-MHz NMR transitions are in the upper electron spin level, corresponding to $m_S = +1/2$.

To acquire the complete hyperfine-level structure for $^{143}\text{Nd}^{3+}$ with $I = 7/2$, the NMR transitions that are unreachable by standard pulsed ENDOR experiments are further investigated with a generalized Davies ENDOR technique. Single spin flips during the preparation and mixing steps in a traditional Davies ENDOR sequence [12,35] can be revised into successive multiple spin flips to access NMR transitions that do not share a common energy level with the selected EPR transition. These transitions of $|m_S, m_I\rangle \rightarrow |m_S, m_I + 1\rangle$, with $m_I < +1/2$ ($m_I > +3/2$), can be detected in a step-by-step manner once the resonance frequencies of $|m_S, m'_I\rangle \rightarrow |m_S, m'_I + 1\rangle$, with $m_I < m'_I \leq +1/2$ ($m_I > m'_I \geq +3/2$), have been determined. Two sequences are given in Fig. 5 as examples. A graphical illustration is given in Fig. S2 in Supplemental Material [31]. In the preparation step, the population is pumped from $| -1/2, m'_I\rangle$ to $| +1/2, m_I - m'_I + 1/2\rangle$ for $m'_I = +3/2, -1/2, \dots, m_I + 2$, and $m_I + 1$, successively. In the mixing step, in which the radio frequency is swept, the EPR transition is depolarized by the population transfer from $|m_S, m_I\rangle$, in which m_S can be deliberately chosen to be either $+1/2$ or $-1/2$. In the detection step, the spin-echo intensity is monitored to produce the ENDOR spectra. The “Tidy” pulse can also be generalized to the pulse sequence. By compulsively initializing the population distribution among the hyperfine energy levels, the reduction of the ENDOR-signal intensity due to the slow nuclear spin relaxation can be effectively avoided [36].

In Fig. 5(c), two ENDOR lines of the NMR transitions $|\pm 1/2, -1/2\rangle \rightarrow |\pm 1/2, +1/2\rangle$ are given. In principle the specific ENDOR line corresponding to $m_S = +1/2$ or $m_S = -1/2$ should appear in only one of the two spectra. One specific ENDOR sequence is designed for one specific NMR transition. This is different from standard Davies ENDOR experiments. The analysis of the correspondence of a particular ENDOR line to a certain electron spin projection m_S is therefore simplified.

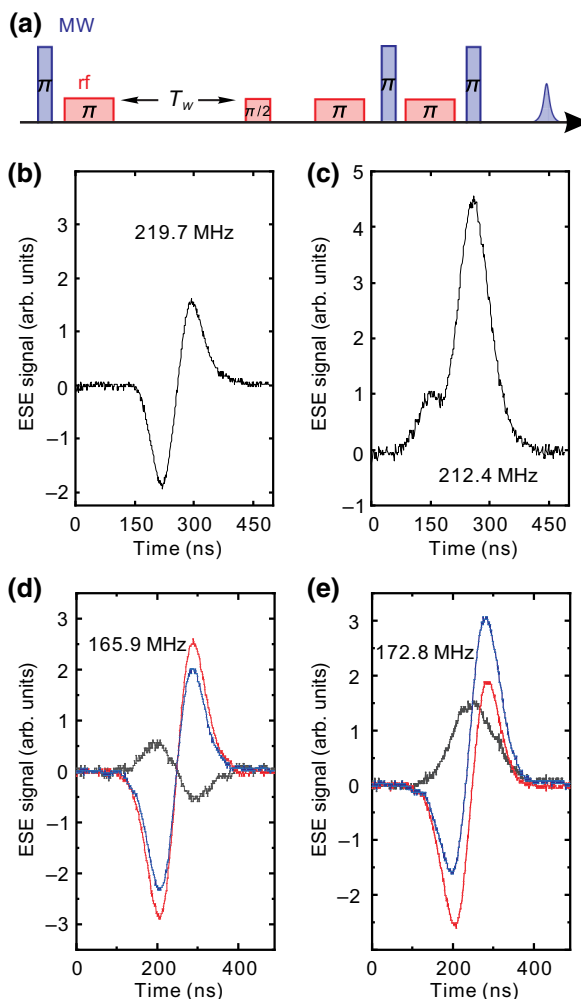


FIG. 4. (a) Pulse sequence applied to determine the correspondence of the NMR lines to the electron spin projection m_S . This sequence can also be used to measure T_{1n} by varying T_W while $T_{1e} \ll T_W \ll T_{1n}$ is satisfied. (b)–(e) Spin-echo signal recorded at the end of the sequence presented in (a) when the radio frequency (rf) is set to 219.7, 212.4, 165.9, and 172.8 MHz, respectively. In (d),(e) The echo signals recorded with (shown in blue) and without (shown in red) the initial nuclear spin polarization and the difference between them (shown in gray). MW, microwave.

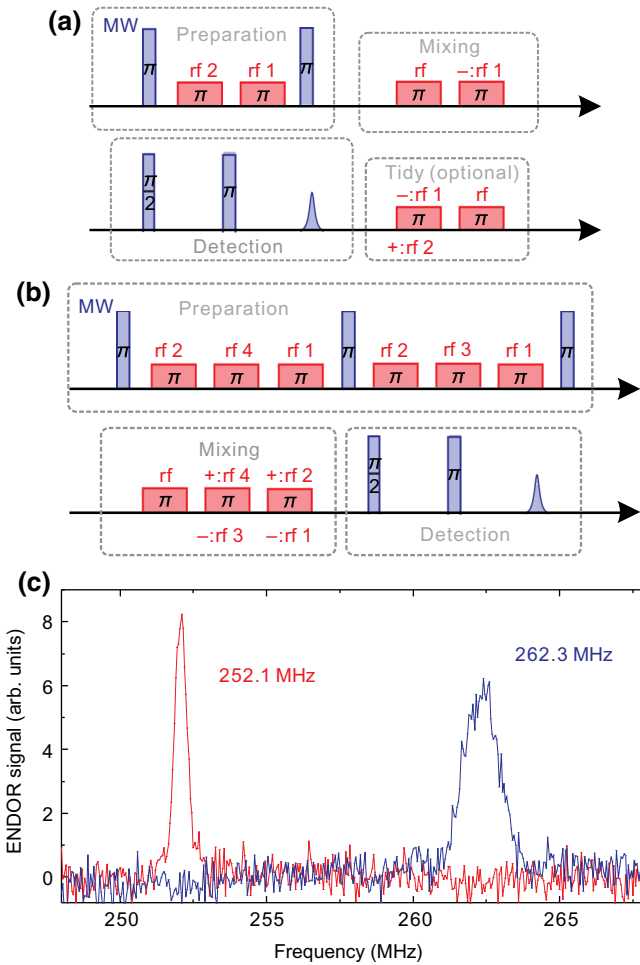


FIG. 5. (a) Pulse sequence used to search for the NMR transitions $|m_s, -1/2\rangle \rightarrow |m_s, +1/2\rangle$. (b) Pulse sequence used to search for the NMR transitions $|m_s, -3/2\rangle \rightarrow |m_s, -1/2\rangle$. Here m_s can be either $-1/2$ (to choose “ $-$ ” in the figures) or $+1/2$ (to choose “ $+$ ” in the figures). Rf 1, rf 2, rf 3, and rf 4 correspond to excitation frequencies of 212.4, 219.7, 172.8, and 165.9 MHz, respectively, and rf represents the frequency to be swept. (c) ENDOR signals corresponding to $| -1/2, -1/2\rangle \rightarrow | -1/2, +1/2\rangle$ (shown in red) and $| +1/2, -1/2\rangle \rightarrow | +1/2, +1/2\rangle$ (shown in blue). MW, microwave.

The effect of the generalized “Tidy” sequence is shown in Fig. 6. In addition, with the variation of the rf-pulse length as illustrated in Fig. 7(a), the Rabi oscillation of an NMR transition that is unreachable with the conventional pulsed ENDOR technique can be observed. The result is given in Fig. 7(b), demonstrating the ability to coherently manipulate all of the NMR transitions with $\Delta m_I = 1$.

All other relevant ENDOR signals corresponding to the transitions with $\Delta m_S = 0$ and $\Delta m_I = 1$ are shown in Fig. S3 in Supplemental Material [31]. After gathering the results from these ENDOR signals, we generate a complete energy-level diagram, which is given in Fig. 8.

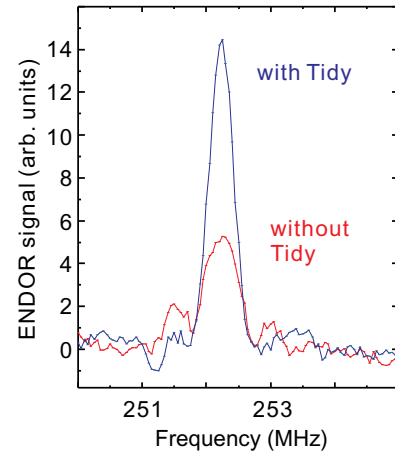


FIG. 6. The ENDOR signal at 252.1 MHz measured with and without the “Tidy” sequence. The ENDOR signal is acquired at approximately 6 K. The experimental repetition time is 20 ms, and the average number is set as 50.

IV. RECONSTRUCTION OF THE SPIN HAMILTONIAN

To make a comparison, we reconstruct the spin Hamiltonian to predict the hyperfine-level structure. This Hamiltonian is also useful in the analysis of the decoherence mechanisms in Sec. V. The spin Hamiltonian takes the form

$$H = \beta \mathbf{B}_0 \cdot \mathbf{g} \cdot \mathbf{S} + \mathbf{I} \cdot \mathbf{A} \cdot \mathbf{S}, \quad (1)$$

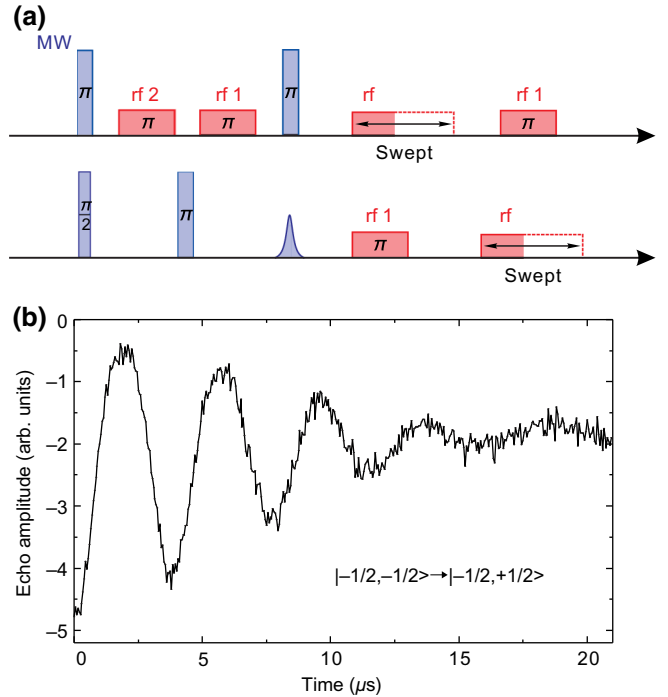


FIG. 7. (a) The pulse sequence applied to detect the Rabi oscillation of the NMR transition $| \pm 1/2, -1/2\rangle \rightarrow | \pm 1/2, +1/2\rangle$, with its experimental result given in (b). MW, microwave.

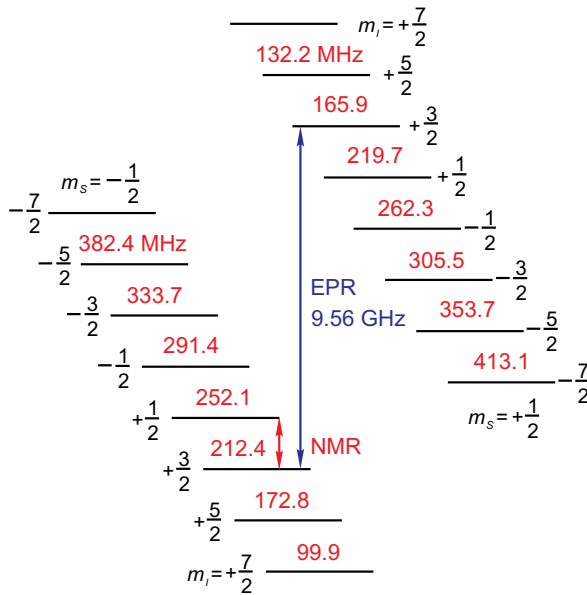


FIG. 8. Complete energy-level structure of the ground state ${}^4\text{I}_{9/2}(0)$ of ${}^{143}\text{Nd}^{3+}:\text{Y}_2\text{SiO}_5$ as determined with the pulsed ENDOR technique.

where β is the Bohr magneton, \mathbf{g} and \mathbf{A} are the g and hyperfine tensors, respectively, and \mathbf{S} (\mathbf{I}) denotes the electron (nuclear) spin operator.

Three pieces of crystals with dimensions of $13 \times 2.1 \times 2.1 \text{ mm}^3$ are used here. They are cut along the D_1 , D_2 , and b axes, while the 13-mm orientation is different for each of the crystals. Field-swept ESE experiments are performed when the crystals are rotated around the 13-mm orientation in increments of 5° . Nd^{3+} ions can substitute for Y^{3+} ions located at two of the crystallographic sites, referred to as “site I” and “site II” [37]. However, in most cases, only the EPR lines from site I can be completely gathered, possibly because the Nd^{3+} dopants preferentially occupy site I [7]. When \mathbf{B}_0 has an arbitrary orientation with respect to the crystal (i.e., not parallel or perpendicular to the b axis), each of the sites can be divided into two magnetically inequivalent classes. This can lead to two sets of EPR signals as displayed in each of the plots in Fig. 9. Nevertheless, during the fitting process for each of the crystal orientations, the resonant magnetic field positions are recorded in order from small to large, regardless of the different magnetic inequivalent sites.

A program based on the EasySpin software package [38] is used for the fitting process. When a group of g and A matrices is generated by the program, the peak positions are calculated and arranged also in order from small to large. These calculated results are then compared with the experimental data. Assignment of the peaks to the particularly predicted lines is not needed. Ultimately, an average deviation of 18.4 G for a single experimental data point is achieved. The best-fit \mathbf{g} matrix in the D_2 - b - D_1 crystal

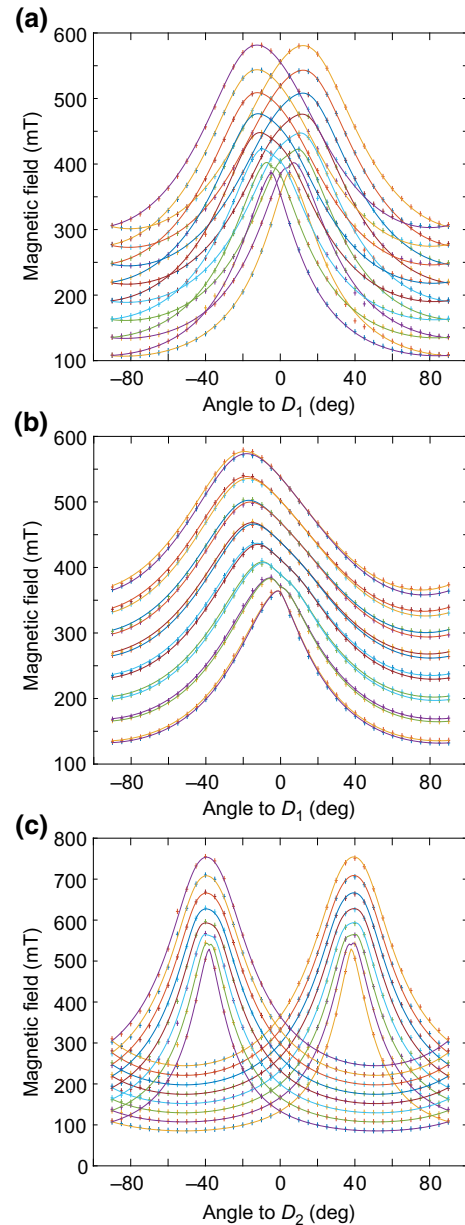


FIG. 9. Angular variations of the EPR peaks of ${}^{143}\text{Nd}^{3+}:\text{Y}_2\text{SiO}_5$. The magnetic field B_0 varies on the b - D_1 (a), D_1 - D_2 (b), and b - D_2 (c) planes. The fitted results are represented by solid lines.

frame is as follows:

$$\mathbf{g} = \begin{pmatrix} -1.03 & -2.48 & 0.44 \\ -2.49 & -2.19 & -0.14 \\ 0.44 & -0.14 & 1.39 \end{pmatrix}.$$

The principal values are $g_x = -4.16$, $g_y = 0.68$, and $g_z = 1.65$. The corresponding Euler angles (Z-Y-Z convention) are $\alpha = 87^\circ$, $\beta = 149^\circ$, and $\theta = 36^\circ$, which describe the transformation from the principal axis frame to the D_2 - b - D_1 crystal frame.

The best-fit \mathbf{A} matrix in the D_2 - b - D_1 frame (in mega-hertz) is as follows:

$$\mathbf{A} = \begin{pmatrix} 495.7 & 687.4 & -232.8 \\ 687.4 & 751.8 & 165.8 \\ -232.8 & 165.8 & -338.3 \end{pmatrix}.$$

The principal values are $A_x = 1323$, $A_y = -520$, and $A_z = -137$ MHz, and the corresponding Euler angles (Z-Y-Z convention) are $\alpha = 91^\circ$, $\beta = 122^\circ$, and $\theta = -140^\circ$.

On the basis of the reconstructed spin Hamiltonian, simulation shows that when the EPR spectrum in Fig. 3(a) is generated, using the language of the spherical coordinate system, the orientation of \mathbf{B}_0 is $(\theta, \phi) = (-2.24^\circ, -66.35^\circ)$ with respect to (D_2, b, D_1) .

The level structure simulated at $B_0 = 402.7$ mT with the spin Hamiltonian is coincident with our measured level structure with deviations from approximately 1 MHz to approximately 30 MHz. The advantage of the accuracy of our modified ENDOR technique is shown.

V. COHERENT ELECTRON AND NUCLEAR SPIN DYNAMICS

A comparison of T_{1e} and the nuclear spin relaxation time T_{1n} recorded at $B_0 = 402.7$ mT is given in Fig. 10. T_{1e} is measured by inversion-recovery experiments. T_{1n} is measured with the sequence presented in Fig. 4(a). The microwave and rf π pulses are 52 ns and $1.08 \mu\text{s}$ in length, respectively. For a coupled electron-nuclear spin system, the relaxation route can be more complicated compared with a simple spin-1/2 system. After the π -pulse excitation at the beginning of the inversion-recovery sequence, the population can, as usual, drop directly to the energy level with the same nuclear spin projection m_I , or it can drop

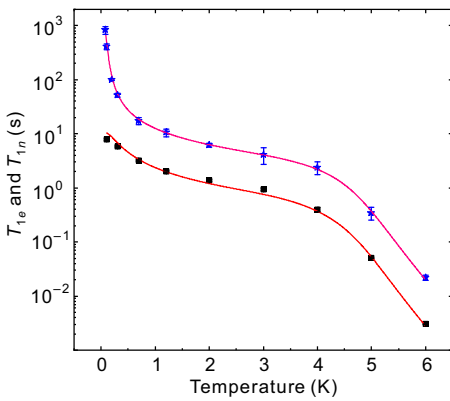


FIG. 10. Temperature dependence of the electron and nuclear spin relaxation times recorded at $B_0 = 402.7$ mT. The measured T_{1n} values are shown as blue stars. The NMR transition $| -1/2, +1/2 \rangle \rightarrow | -1/2, +3/2 \rangle$ (212.4 MHz) is investigated here. The T_{1e} data are shown as black squares. The solid lines are the corresponding fitted curves.

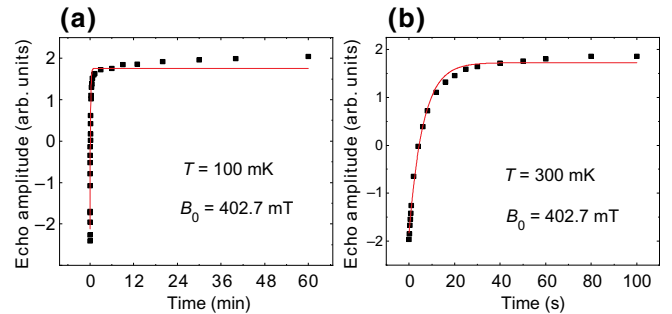


FIG. 11. Inversion-recovery curves measured for $^{143}\text{Nd}^{3+}$: Y_2SiO_5 at temperatures lower than 500 mK. The solid lines are single-exponential fits.

first to levels with different m_I , and then take a long time to come back via nuclear spin relaxation. It is observed that when the sample temperature is lower than 500 mK, single-exponential fits cannot work well; see Fig. 11.

However, when the temperature is higher than 500 mK, single-exponential fits are quite good. The significant change that happens below the electronic Zeeman temperature seems to be due to the rapid increase of the ratio between the electron and nuclear spin relaxation rates, but further investigation is required. For completeness, the electron spin relaxation times displayed in Fig. 10 are the results of single-exponential fits over the full temperature range.

For $^{143}\text{Nd}^{3+}$, nuclear spin relaxation is dominated by the rapid relaxation of the electron spins at temperatures above the electronic Zeeman temperature of $hf_r/k_B \sim 460$ mK. This behavior manifests itself as a constant ratio σ between the two relaxation rates [30], which is obvious in Fig. 10. However, as the temperature decreases, the electron spins start to freeze out, and the much slower SLR of the nuclear spins themselves starts to take over. The nuclear spin relaxation can thus be modeled as follows [39,40]:

$$T_{1n}^{-1} = \sigma(1 - P_e^2)T_{1e}^{-1} + \gamma_d \coth\left(\frac{hf_n}{2k_B T}\right) + \gamma_R T^9 + \gamma_O f_r^3 \exp\left(-\frac{hf_r}{k_B T}\right), \quad (2)$$

where f_n represents the NMR transition frequency of 212.4 MHz, and γ_d , γ_R , and γ_O are the coupling factors of the direct, Raman, and Orbach processes, respectively. The ratio σ is fitted to be 0.126. The coupling factors for direct and Orbach processes are fitted as $\gamma_d = 7.3 \times 10^{-5} \text{ s}^{-1}$ and $\gamma_O = 1 \times 10^{-32} \text{ Hz}^{-2}$, while the impact of the Raman process is found to be negligible. The T_{1n} data show excellent agreement with the fitted curve. Moreover, there is a strong temperature dependence for T_{1n} even below 100 mK. T_{1n} of 13.8 ± 2.3 min is obtained at 75 mK, which is much longer compared with the lifetime of the optically excited

state of approximately $300 \mu\text{s}$ [41]. This is highly profitable for efficient optical pumping and long-term quantum storage using $^{143}\text{Nd}^{3+}:\text{Y}_2\text{SiO}_5$ [4,18].

The study of T_{2e} is conducted during the second period of cooling, with use of the same EPR transition. The temperature dependence of T_{2e} is given in Fig. 12 along with the fitted curve based on the model discussed in detail in Supplemental Material [31]. Spectral diffusion (SD) caused by electronic SLR-induced random spin flips is the main source of decoherence for the electron and nuclear spins. The dipolar half-width of the electron spin can be estimated to be approximately 5 kHz, which is much smaller than the inhomogeneous broadening of approximately 25 MHz. Therefore, the decoherence induced by electronic spin flip-flops can be omitted. The decay of spin echoes therefore follows the Mims decay law [42], taking the form $\exp[-(2\tau/T_2)^m]$. In Y_2SiO_5 the Nd^{3+} ions preferentially occupy one of the Y^{3+} crystallographic sites [7], but as shown in Fig. S4 in Supplemental Material [31], the impact of the dopant ions located at the other site should not be ignored. This can lead to inaccuracy in the modeling. When the temperature is reduced, the SLR rate will slow down, and the electron spins can eventually be frozen out. As a result, the electronic SLR-induced decoherence effect can be gradually inhibited. To alleviate the instantaneous-diffusion (ID) effect that results from the compulsory electron spin flips following the refocusing pulse in a two-pulse Hahn-echo sequence [43], here soft pulses are used in the T_{2e} measurements [44]. The microwave peak power is set to 75 mW and the nominal

π pulses are 700 ns. At 100 mK, T_{2e} of 2.18 ± 0.09 ms is obtained with a reduced refocusing pulse of 200 ns. The stretch factor is $m = 1.42 \pm 0.09$. This is a remarkable result obtained for rare-earth ions without the assistance of a clock transition, and it is comparable to results for other solid-state electron spin systems such as defects in diamonds and in SiC.

The temperature dependence of T_{2n} is also shown in Fig. 12 along with the fitted curve based on Eq. (5) in Supplemental Material [31]. T_{2n} is measured by converting nuclear spin echoes into ESE [6]. T_{2n} of 43 ± 7 ms with a stretch factor of $m = 1.65 \pm 0.24$ is obtained at 100 mK. Once the electron spins have been frozen out, T_{2n} is ultimately limited by the flip-flops of the host nuclear spins. From the effective spin Hamiltonian (see Supplemental Material [31]), the gradient of the NMR transition frequency with respect to the external magnetic field can be calculated as 160 MHz/T. Considering the flip-flops among the bulk ^{89}Y spins far from the central Nd^{3+} ions, T_{2n} can be accordingly estimated to be approximately 250 μs . However, the experimentally measured T_{2n} is more than 2 orders of magnitude longer. This is caused by the frozen core effect induced by the large magnetic moment of the central Nd^{3+} electron spins [4,45]. Strong hyperfine coupling between the central electron spin and each of the neighboring host nuclear spins can cause detuning among the host nuclear spins. The resonant flip-flops can thus be heavily suppressed.

To further extend the coherence lifetime of the electron spin, besides the impacts of the host nuclear spins, at least two limiting factors need to be considered. The first one is

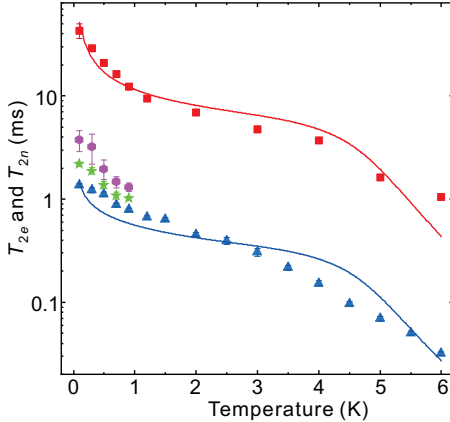


FIG. 12. Temperature dependence of the electron and nuclear spin coherence times recorded at $B_0 = 402.7$ mT. The measured T_{2n} values are shown as red squares. The solid red line is the fitted curve. T_{2e} values measured with soft pulses and the nominal flipping angles of π are shown as blue triangles. The solid blue line is the fitted curve. The green stars represent T_{2e} data measured with refocusing pulses of 200 ns. These measurements are conducted below 1 K for a high single-to-noise ratio. The purple hexagons represent the deduced T_{2e} values, from which the ID effect has been eliminated.

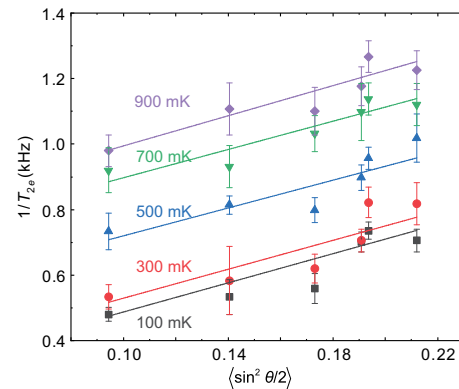


FIG. 13. Demonstration of the instantaneous-diffusion effect. $1/T_{2e}$ is plotted as a function of the average spin-flip probability $(\sin^2 \theta/2)$. T_{2e} is measured at $B_0 = 402.7$ mT with a pulse sequence of $\pi/2-\tau-\theta-\tau$ -echo, in which θ represents the effective rotation angle of the refocusing pulse. The value of $(\sin^2 \theta/2)$ is calculated with Eq. (4) in Supplemental Material [31]. The microwave power is set to approximately 75 mW, and the refocusing-pulse lengths are varied. Experiments are conducted at five different temperatures below 1 K. The solid lines are the linear fits.

the remaining ID effect. With a reduced refocusing pulse of 200 ns, the ID effect can still account for $T_{2e, ID}$ of 5.1 ms as indicated in Fig. 13.

Secondly, when T_{2e} is being measured in an electron spin ensemble, all of the resonant electron spins are excited, and these electron spins are no longer polarized. At 100 mK this would result in $T_{2e, SD} \approx 10.5$ ms. These two effects can be minimized in a low-doping sample, or even better, in single-ion systems [23]. To overcome the superhyperfine limit for both the dopant electron and nuclear spins, in principle the most-efficient way is to use a host material with much-lower nuclear-spin concentration [46,47]. Otherwise, the detrimental effect of the host nuclear spins should be somehow inhibited. For example, the zero-order Zeeman technique and dynamical decoupling can be applied for the microwave and rf transitions [8,45]. Since the spin relaxation times are on the minute scale, and currently the coherence time is limited by nuclear spin flip-flops, with a high-quality dynamical decoupling sequence, a coherence time on the second scale should be achievable [48,49].

VI. SUMMARY AND CONCLUSION

In conclusion, comprehensive enhancement of the population and coherence lifetimes is achieved in the subkelvin-temperature regime for both electron and nuclear spins, with compatibility of high-quality and fast manipulations [31]. The pulsed ENDOR protocol used for hyperfine-structure characterization can also be generalized to other spin systems for which the spin Hamiltonians are hard to be precisely determined [10,50] and those without an auxiliary optical transition.

In addition, the compatibility of the subkelvin sample temperature with a conventional three-dimensional ENDOR resonator makes the platform suitable for ordinary EPR samples in various research fields. For example, it is also promising to enhance the coherent properties of molecular nanomagnets [51,52]. More intrinsically, the duration of a pulsed EPR experiment should be less than the spin relaxation time, which is typically highly dependent on the sample temperature. Therefore, with a wider working temperature range, broader options for the samples and the experimental pulse sequences can be expected. For instance, a rapid increase of the nuclear spin relaxation time at subkelvin temperatures, as observed in this study, is possible to provide some previously inaccessible ENDOR signals for [NiFe] hydrogenase [53], and for the Mn cluster in photosystem II [54]. Besides, a high degree of electron spin polarization at subkelvin temperatures can also lead to an opportunity for investigation of the ground spin state [55,56] and a complete characterization to the hyperfine coupling constants [57].

ACKNOWLEDGMENTS

This work was supported by the National Key R&D Program of China (Grant No. 2017YFA0304100), the National Natural Science Foundation of China (Grants No. 11774331, No. 11774335, 11504362, No. 11821404, and No. 11654002), the Anhui Initiative in Quantum Information Technologies (Grant No. AHY020100), the Key Research Program of Frontier Sciences, Chinese Academy of Sciences (Grant No. QYZDY-SSW-SLH003), the Science Foundation of the Chinese Academy of Sciences (Grant No. ZDRW-XH-2019-1), and the Fundamental Research Funds for the Central Universities (Grant No. WK2470000026).

- [1] Z.-L. Xiang, S. Ashhab, J. You, and F. Nori, Hybrid quantum circuits: Superconducting circuits interacting with other quantum systems, *Rev. Mod. Phys.* **85**, 623 (2013).
- [2] X. Zhu, S. Saito, A. Kemp, K. Kakuyanagi, S.-I. Kamimoto, H. Nakano, W. J. Munro, Y. Tokura, M. S. Everitt, K. Nemoto *et al.*, Coherent coupling of a superconducting flux qubit to an electron spin ensemble in diamond, *Nature* **478**, 221 (2011).
- [3] S. Probst, H. Rotzinger, S. Wünsch, P. Jung, M. Jerger, M. Siegel, A. Ustinov, and P. Bushev, Anisotropic Rare-Earth Spin Ensemble Strongly Coupled to a Superconducting Resonator, *Phys. Rev. Lett.* **110**, 157001 (2013).
- [4] M. Rančić, M. P. Hedges, R. L. Ahlefeldt, and M. J. Sellars, Coherence time of over a second in a telecom-compatible quantum memory storage material, *Nat. Phys.* **14**, 50 (2018).
- [5] M. Steger, K. Saeedi, M. Thewalt, J. Morton, H. Riemann, N. Abrosimov, P. Becker, and H.-J. Pohl, Quantum information storage for over 180 s using donor spins in a ^{28}Si “semiconductor vacuum”, *Science* **336**, 1280 (2012).
- [6] J. J. Morton, A. M. Tyryshkin, R. M. Brown, S. Shankar, B. W. Lovett, A. Ardavan, T. Schenkel, E. E. Haller, J. W. Ager, and S. Lyon, Solid-state quantum memory using the ^{31}P nuclear spin, *Nature* **455**, 1085 (2008).
- [7] G. Wolfowicz, H. Maier-Flaig, R. Marino, A. Ferrier, H. Vezin, J. J. Morton, and P. Goldner, Coherent Storage of Microwave Excitations in Rare-Earth Nuclear Spins, *Phys. Rev. Lett.* **114**, 170503 (2015).
- [8] A. Ortú, A. Tiranov, S. Welinski, F. Fröwis, N. Gisin, A. Ferrier, P. Goldner, and M. Afzelius, Simultaneous coherence enhancement of optical and microwave transitions in solid-state electronic spins, *Nat. Mater.* **17**, 671 (2018).
- [9] M. Afzelius, C. Simon, H. De Riedmatten, and N. Gisin, Multimode quantum memory based on atomic frequency combs, *Phys. Rev. A* **79**, 052329 (2009).
- [10] E. Saglamyurek, J. Jin, V. B. Verma, M. D. Shaw, F. Marsili, S. W. Nam, D. Oblak, and W. Tittel, Quantum storage of entangled telecom-wavelength photons in an erbium-doped optical fibre, *Nat. Photon.* **9**, 83 (2015).
- [11] H.-J. Lim, S. Welinski, A. Ferrier, P. Goldner, and J. Morton, Coherent spin dynamics of ytterbium ions in yttrium orthosilicate, *Phys. Rev. B* **97**, 064409 (2018).

- [12] A. Schweiger and G. Jeschke, *Principles of Pulse Electron Paramagnetic Resonance* (Oxford University Press on Demand, New York, 2001).
- [13] G. Feher and E. Gere, Electron spin resonance experiments on donors in silicon. II. Electron spin relaxation effects, *Phys. Rev.* **114**, 1245 (1959).
- [14] C. Clausen, I. Usmani, F. Bussières, N. Sangouard, M. Afzelius, H. de Riedmatten, and N. Gisin, Quantum storage of photonic entanglement in a crystal, *Nature* **469**, 508 (2011).
- [15] T. Zhong, J. M. Kindem, J. G. Bartholomew, J. Rochman, I. Craiciu, E. Miyazono, M. Bettinelli, E. Cavalli, V. Verma, S. W. Nam *et al.*, Nanophotonic rare-earth quantum memory with optically controlled retrieval, *Science* **357**, 1392 (2017).
- [16] F. Bussières, C. Clausen, A. Tiranov, B. Korzh, V. B. Verma, S. W. Nam, F. Marsili, A. Ferrier, P. Goldner, H. Herrmann *et al.*, Quantum teleportation from a telecom-wavelength photon to a solid-state quantum memory, *Nat. Photon.* **8**, 775 (2014).
- [17] Z.-Q. Zhou, W.-B. Lin, M. Yang, C.-F. Li, and G.-C. Guo, Realization of Reliable Solid-State Quantum Memory for Photonic Polarization Qubit, *Phys. Rev. Lett.* **108**, 190505 (2012).
- [18] J.-S. Tang, Z.-Q. Zhou, Y.-T. Wang, Y.-L. Li, X. Liu, Y.-L. Hua, Y. Zou, S. Wang, D.-Y. He, G. Chen *et al.*, Storage of multiple single-photon pulses emitted from a quantum dot in a solid-state quantum memory, *Nat. Commun.* **6**, 8652 (2015).
- [19] M. P. Hedges, J. J. Longdell, Y. Li, and M. J. Sellars, Efficient quantum memory for light, *Nature* **465**, 1052 (2010).
- [20] L. A. Williamson, Y.-H. Chen, and J. J. Longdell, Magneto-Optic Modulator with Unit Quantum Efficiency, *Phys. Rev. Lett.* **113**, 203601 (2014).
- [21] C. O'Brien, N. Lauk, S. Blum, G. Morigi, and M. Fleischhauer, Interfacing Superconducting Qubits and Telecom Photons via a Rare-Earth-Doped Crystal, *Phys. Rev. Lett.* **113**, 063603 (2014).
- [22] N. Kukharchyk, D. Sholokhov, O. Morozov, S. Korableva, A. Kalachev, and P. Bushev, Optical coherence of ^{166}Er : $^7\text{LiYF}_4$ crystal below 1 K, *New J. Phys.* **20**, 023044 (2018).
- [23] T. Zhong, J. M. Kindem, J. G. Bartholomew, J. Rochman, I. Craiciu, V. Verma, S. W. Nam, F. Marsili, M. D. Shaw, A. D. Beyer *et al.*, Optically Addressing Single Rare-Earth Ions in a Nanophotonic Cavity, *Phys. Rev. Lett.* **121**, 183603 (2018).
- [24] S. Probst, H. Rotzinger, A. Ustinov, and P. Bushev, Microwave multimode memory with an erbium spin ensemble, *Phys. Rev. B* **92**, 014421 (2015).
- [25] J. M. Kindem, J. G. Bartholomew, P. J. Woodburn, T. Zhong, I. Craiciu, R. L. Cone, C. W. Thiel, A. Faraon, Characterization of $^{171}\text{Yb}^{3+}$: YVO_4 for photonic quantum technologies, *Phys. Rev. B* **98**, 024404 (2018).
- [26] G. A. Slack, Thermal conductivity of pure and impure silicon, silicon carbide, and diamond, *J. Appl. Phys.* **35**, 3460 (1964).
- [27] A. J. Sigillito, A. M. Tyryshkin, T. Schenkel, A. A. Houck, and S. A. Lyon, All-electric control of donor nuclear spin qubits in silicon, *Nat. Nanotechnol.* **12**, 958 (2017).
- [28] E. Z. Cruzeiro, A. Tiranov, I. Usmani, C. Laplane, J. Lavoie, A. Ferrier, P. Goldner, N. Gisin, and M. Afzelius, Spectral hole lifetimes and spin population relaxation dynamics in neodymium-doped yttrium orthosilicate, *Phys. Rev. B* **95**, 205119 (2017).
- [29] C. Kutter, H. Moll, J. Van Tol, H. Zuckermann, J. Maan, and P. Wyder, Electron-Spin Echoes at 604 GHz Using Far Infrared Lasers, *Phys. Rev. Lett.* **74**, 2925 (1995).
- [30] C. D. Jeffries, *Dynamic Nuclear Orientation* (Interscience, New York, 1963).
- [31] See Supplemental Material at <http://link.aps.org/supplemental/10.1103/PhysRevApplied.13.024080> for illustrations of the ENDOR sequences and details of the studies of the coherent electron and nuclear spin dynamics. Here Ref. [32] is included.
- [32] A. G. Maryasov, S. A. Dzuba, and K. M. Salikhov, Spin-polarization effects on the phase relaxation induced by dipole-dipole interactions, *J. Magn. Reson.* (1969) **50**(3), 432 (1982).
- [33] J. A. Weil and J. R. Bolton, *Electron Paramagnetic Resonance: Elementary Theory and Practical Applications* (John Wiley & Sons, Hoboken, New Jersey, 2007).
- [34] O. Guillot-Noël, P. Goldner, Y. Le Du, E. Baldit, P. Monnier, and K. Bencheikh, Hyperfine interaction of Er^{3+} ions in Y_2SiO_5 : An electron paramagnetic resonance spectroscopy study, *Phys. Rev. B* **74**, 214409 (2006).
- [35] E. Davies, A new pulse endor technique, *Phys. Lett. A* **47**, 1 (1974).
- [36] A. M. Tyryshkin, J. J. Morton, A. Ardavan, and S. Lyon, Davies electron-nuclear double resonance revisited: Enhanced sensitivity and nuclear spin relaxation, *J. Chem. Phys.* **124**, 234508 (2006).
- [37] R. Beach, M. D. Shinn, L. Davis, R. W. Solarz, and W. F. Krupke, Optical absorption and stimulated emission of neodymium in yttrium orthosilicate, *IEEE J. Quantum Electron.* **26**, 1405 (1990).
- [38] S. Stoll and A. Schweiger, Easyspin, a comprehensive software package for spectral simulation and analysis in EPR, *J. Magn. Reson.* **178**, 42 (2006).
- [39] J. Waugh and C. P. Slichter, Mechanism of nuclear spin-lattice relaxation in insulators at very low temperatures, *Phys. Rev. B* **37**, 4337 (1988).
- [40] A. Abragam and B. Bleaney, *Electron Paramagnetic Resonance of Transition Metal Ions* (Dover, Dover, 1970), 2nd ed., Chap. 10.
- [41] I. Usmani, M. Afzelius, H. De Riedmatten, and N. Gisin, Mapping multiple photonic qubits into and out of one solid-state atomic ensemble, *Nat. Commun.* **1**, 12 (2010).
- [42] W. Mims, Phase memory in electron spin echoes, lattice relaxation effects in CaWO_4 : Er, Ce, Mn, *Phys. Rev.* **168**, 370 (1968).
- [43] J. Klauder and P. Anderson, Spectral diffusion decay in spin resonance experiments, *Phys. Rev.* **125**, 912 (1962).
- [44] S. A. Dzuba and A. Kawamori, Selective hole burning in EPR: Spectral diffusion and dipolar broadening, *Concepts Magn. Reson.* **8**, 49 (1996).
- [45] M. Zhong, M. P. Hedges, R. L. Ahlefeldt, J. G. Bartholomew, S. E. Beavan, S. M. Wittig, J. J. Longdell, and M. J. Sellars, Optically addressable nuclear spins in a solid with a six-hour coherence time, *Nature* **517**, 177 (2015).

- [46] A. M. Tyryshkin, S. Tojo, J. J. Morton, H. Riemann, N. V. Abrosimov, P. Becker, H.-J. Pohl, T. Schenkel, M. L. Thewalt, K. M. Itoh *et al.*, Electron spin coherence exceeding seconds in high-purity silicon, *Nat. Mater.* **11**, 143 (2012).
- [47] C. M. Phenicie, P. Stevenson, S. Welinski, B. C. Rose, A. T. Asfaw, R. J. Cava, S. A. Lyon, N. P. de Leon, and J. D. Thompson, Narrow optical linewidths in erbium implanted in TiO₂, [arXiv:1909.06304](#) (2019).
- [48] N. Bar-Gill, L. M. Pham, A. Jarmola, D. Budker, and R. L. Walsworth, Solid-state electronic spin coherence time approaching one second, *Nat. Commun.* **4**, 1 (2013).
- [49] B. C. Rose, D. Huang, Z.-H. Zhang, P. Stevenson, A. M. Tyryshkin, S. Sangtawesin, S. Srinivasan, L. Loudin, M. L. Markham, A. M. Edmonds *et al.*, Observation of an environmentally insensitive solid-state spin defect in diamond, *Science* **361**, 60 (2018).
- [50] Y.-H. Chen, X. Fernandez-Gonzalvo, S. P. Horvath, J. V. Rakonjac, and J. J. Longdell, Hyperfine interactions of Er³⁺ ions in Y₂SiO₅: Electron paramagnetic resonance in a tunable microwave cavity, *Phys. Rev. B* **97**, 024419 (2018).
- [51] S. J. Melhuish, C. Stott, A.-M. Ariciu, L. Martinis, M. McCulloch, L. Piccirillo, D. Collison, F. Tuna, and R. Winpenny, A sub-Kelvin cryogen-free EPR system, *J. Magn. Reson.* **282**, 83 (2017).
- [52] M. Shiddiq, D. Komijani, Y. Duan, A. Gaita-Ariño, E. Coronado, and S. Hill, Enhancing coherence in molecular spin qubits via atomic clock transitions, *Nature* **531**, 348 (2016).
- [53] S. Foerster, M. Van Gastel, M. Brecht, and W. Lubitz, An orientation-selected endor and hyscore study of the Ni-C active state of desulfovibrio vulgaris miyazaki F hydrogenase, *J. Biol. Inorg. Chem.* **10**, 51 (2005).
- [54] L. Jin, P. Smith, C. J. Noble, R. Stranger, G. R. Hanson, and R. J. Pace, Electronic structure of the oxygen evolving complex in photosystem II, as revealed by ⁵⁵Mn davies endor studies at 2.5 K, *Phys. Chem. Chem. Phys.* **16**, 7799 (2014).
- [55] J. Yang, Y. Wang, Z. Wang, X. Rong, C.-K. Duan, J.-H. Su, and J. Du, Observing Quantum Oscillation of Ground States in Single Molecular Magnet, *Phys. Rev. Lett.* **108**, 230501 (2012).
- [56] S. Bertaina, S. Gambarelli, T. Mitra, B. Tsukerblat, A. Müller, and B. Barbara, Quantum oscillations in a molecular magnet, *Nature* **453**, 203 (2008).
- [57] D. Baute, D. Arieli, F. Neese, H. Zimmermann, B. M. Weckhuysen, and D. Goldfarb, Carboxylate binding in copper histidine complexes in solution and in zeolite Y: X-and W-band pulsed EPR/ENDOR combined with DFT calculations, *J. Am. Chem. Soc.* **126**, 11733 (2004).